Comparison Assessment of Low Rank Sparse-PCA Based- Clustering/Classification for Automatic Mineral Identification in Long Wave Infrared Hyperspectral Imagery

Bardia Yousefi[a,*], Saeed Sojasi[a], Clemente Ibarra Castanedo[a], Xavier P.V. Maldague[a], Georges Beaudoin[b], Martin Chamberland[c]

[a] *Computer Vision and System Laboratory (CVSL), Department of Electrical and Computer Engineering, Université Laval, 1065, av. de la Médecine, Québec, QC, Canada*
[b] *Department of Geology and Geological Engineering, Université Laval, 1065, av. de la Médecine, Québec, QC, Canada*
[c] *Telops, Inc., 100-2600 St-Jean-Baptiste Ave, Québec, Qc, G2E 6J5, Canada*

Abstract

The developments in hyperspectral technology in different applications are known in many fields particularly in remote sensing, airborne imagery, mineral identification and core logging. The automatic mineral identification system provides considerable assistance in geology to identify mineral automatically. Here, the proposed approach addresses an automated system for mineral (i.e. pyrope, olivine, quartz) identification in the long-wave infrared ($7.7\mu m$ to $11.8\mu m$ - LWIR) ground-based spectroscopy. A low-rank Sparse Principal Component Analysis (Sparse-PCA) based spectral comparison methods such as Spectral Angle Mapper (SAM), Spectral Information Divergence (SID), Normalized Cross Correlation (NCC) have been used to extract the features in the form of false colors composite. Low-rank Sparse-PCA is used to extract the spectral reference which and showed high similarity to the ASTER (JPL/NASA) spectral library. For decision making step, two methods used to establish a comparison

*Corresponding author:
Email addresses: Bardia.Yousefi.1@ulaval.ca (Bardia Yousefi), Saeed.Sojasi.1@ulaval.ca (Saeed Sojasi), IbarraC@gel.ulaval.ca (Clemente Ibarra Castanedo), Xavier.Maldague@gel.ulaval.ca (Xavier P.V. Maldague), Georges.Beaudoin@ggl.ulaval.ca (Georges Beaudoin), martin.chamberland@telops.com (Martin Chamberland)

between a kernel Extreme Learning Machine (ELM) and Principal Component Analysis (PCA) kernel K-means clustering. ELM yields classification accuracy up to 76.69% using SAM based polynomial kernel ELM for pyrope mixture, and 70.95% using SAM based sigmoid kernel ELM for olivine mixture. This accuracy is slightly lower as compared to clustering which yields an identification accuracy of 84.91% (NCC) and 69.9% (SAM). However, the supervised classification significantly depends on the number of training samples and is considerably more difficult as compared to clustering due to labeling and training limitations. Moreover, the results indicate considerable similarity between the spectra from low rank approximation from the spectra of pure sample and the spectra from the ASTER spectral library.

Keywords: `Comparison spectral analysis`, `Hyperspectral infrared image analysis`, `Mineral identification`, `Sparse principal component analysis`, `Extreme learning machine`, `Principal component analysis based K-means clustering`.

This manuscript is an author version and the main article can be found in Infrared Physics Technology Journal [1]. `https://doi.org/10.1016/j.infrared.2018.06.026`

1. Introduction

Technological developments in different wavelength bands in spectroscopy have created interesting opportunities and provide spectral and spatial information from the surface of materials. The automatic/semi-automatic/non-automatic approaches in mineral identification extensively depend on this information. The proposed approach is a ground-based spectroscopy system for automatic mineral identification using extreme learning machine (ELM). It uses spectral comparison to create a false color composite, and the spectral reference is calculated by applying low rank sparse principal component analysis (Sparse-PCA) of the spectra from a mineral's sample. Spectrometric imagery provides

information that can be exclusively used in geological and mineralogical fields [2, 3]. Several spectral databases [e.g. advanced space-borne thermal emission and reflection radiometer (ASTER) [4]] have been widely used as references for spectral analysis and contain a collection of spectral libraries including samples in laboratory or field conditions. The signature of natural materials in such spectral libraries provides opportunities for data mining techniques to be applied to imagery. The spectra from these libraries can serve as reference or ground truth to enable comparison. Recent hyperspectral methods focus on spectral techniques, such as estimating abundance of quartz and clays in oil sand [5] or identifying minerals for mapping [6]. These methods typically compare the targeted spectra in the hyperspectral images with the spectra of minerals in libraries (Cloutis [7] and Plaza et al. [8]). Numerous spectral comparison approaches have been developed and applied for spectral analysis such as SAM and NCC, which are extensively used in the field [4]. For enhanced spectral representation, several features that deal with wavelength position and spectral absorption have been developed.

This study aimed to propose ground-based mineral identification deploying supervised and unsupervised approaches similar to airborne imagery [9, 10, 11] and core logging [12, 13, 14]. The absorption information (signature) and wavelength position depend on the mineral composition and changes based on geochemical information, which can lead to mineral identification [15, 16, 17]. The local and global minima or maxima (extrema) in different wavelengths can be used to distinguish minerals, and this method is becoming a commodity for mineral identification (e.g. effect of lichen in mineral identification [6]).

Short-wave infrared band range is relatively confined [18, 19, 20] compared with other bands, such as visible and near infrared and long-wave infrared (LWIR). This limitation creates difficulties for precise determination of extrema and comparative analysis [9]. Selection of a spectral representative for the identification of pure minerals may involve prior knowledge of physical (e.g. roughness and particle size) and chemical properties of the material, its surface and illumination geometry of measurement (i.e. background continuum, particular albedo

and absorption features) ([21, 22, 23]). Thus, some research is necessary to minimize such effects [21, 24]). Certain approaches have a suitable shape of the known continuum spectra and attempt to fit either locally or entirely in linear or curved baseline approaches ([21, 25]). Spectral comparison methods such as SAM, spectral feature fitting [26] and Tetracorder ([24]) can be applied after continuum removal. The data are sensitive to a variety of factors including the non-uniform thermal property and background reflection of minerals, angle of acquisition and several other parameters. Continuum removal provides a correction to the spectra and prepares the spectra for comparison. This method minimizes the influence of such parameters on the data by removing the continuum from the spectrum. In this study, we studied a set of pure and mixed mineral grains and active thermography, which involves placing a heating source in front of the hyperspectral camera to illuminate samples. Continuum removal uses non-negative factor analysis to find the best spectral representative from downwelling radiation. The analysis of mineral identification uses Sparse-PCA to find the spectra reference and compares findings with the ASTER spectral library [4]. Spectral comparison techniques use these references and create false colors; ultimately, segmentation of the mineral grains is conducted. The proposed approach uses hyperspectral imaging in the wavelength range of 7.7 μm to 11.8 μm (LWIR) for certain mineral grains in laboratory conditions via a FTIR hyperspectral camera equipped with a magnifying lens to improve spatial resolution. The remainder of the paper is organized as follows. In Section 2, we introduce the methodology and explain how continuum removal and segmentation processes are performed. Section 3 describes the experimental and simulation results. We discuss the challenges and advantages of the approach in Section 4. Finally, we conclude and describe future work in Section 5.

2. Method

Here, an automated mineral identification for ground-based spectroscopy is proposed via supervised (ELM) and unsupervised approaches (clustering). To

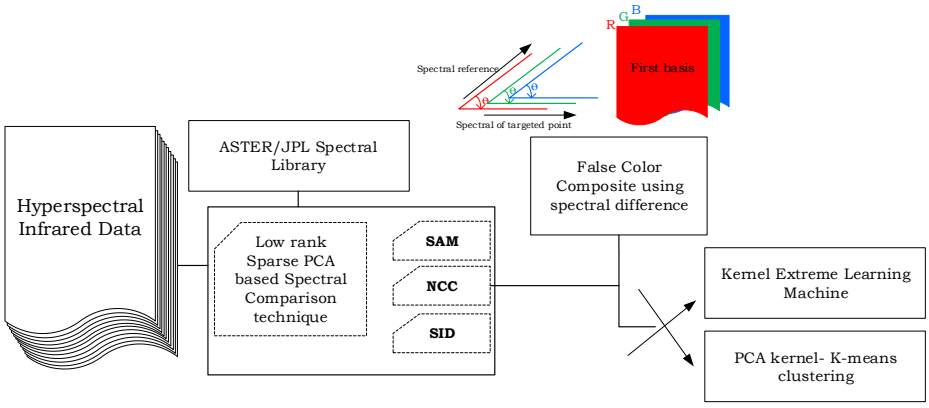

Figure 1: The scheme of the proposed algorithm.

obtain the classification attributes, several spectral comparison techniques were used (i.e. SAM, SID and NCC). To apply spectral comparison techniques, we employed Sparse-PCA to extract the spectral references from single mineral samples and even compared them with ASTER spectral library.

2.1. Spectral Comparison techniques

Spectral Angle Mapper (SAM) calculates the angle between the reference and targeted spectra as an error [27, 28], which represents their physical composition property. It uses the $n - D$ angle to match the targeted spectra to reference spectra. The spectral references for using SAM usually involve spectral libraries, whereas the proposed approach extracted references directly from the spectra of pure samples (such as those presented here). The amount of error generated by SAM represents the significant difference between mineral compositions [27].

Spectral information divergence (SID) is another spectral comparison technique. $x = (x_1, x_2, \ldots x_L)^T$ represents the pixel spectra, X_l component, in hyperspectral data cube, and it is considered a probability distribution aim to estimate the correlation between the spectra (targeted and reference spectra).

$y = (y_1, y_2, \ldots y_L)^T$ is the additional pixel vector that has the probability distribution of $q = \{q_l\}_l^L = 1$ and $q_j = \frac{y_j}{\sum_{l=1}^{L}} y_l$ and composes SID through the following formula:

$$SID(x, y) = D(x||y) + D(y||x) \tag{1}$$

where $p = \{p_l\}_{l=1}^{L}$ is the desired probability vector from the x and $p_j = \frac{x_j}{\sum_{l=1}^{L} x_l}$, and $D(x||y) = \sum_{l=1}^{L} p_l \log(\frac{p_l}{q_l})$. The $D(y||x) = \sum_{l=1}^{L} q_l \log(\frac{p_l}{q_l})$ is the relative entropy or a directed divergence (cross entropy) of x and y through the KullackLeibler function [29].

Normalized Cross Correlation (NCC) involves a simple correlation comparison between the spectra. The images should first be normalized due to many factors such as image brightness variation, exposure conditions and lighting caused by the non-uniform shape of mineral grains. Normalization is performed through division of the mean by standard deviation subtraction. NCC provides a correlation number as valuable information showing the spectral difference between the reference spectrum (similar to SAM, the reference spectra are calculated by the spectral references of pure samples) and targeted spectrum. This method has been used for template matching and image analysis [30].

2.1.1. Sparse-PCA to extract spectral reference

PCA is a linear transformation that can be presented by $S = XL$ (L is an orthonormal basis matrix, and X is a mean-zero data matrix), which maximizes the projected data (S) variance (even hybrid methods such as two-dimensional principal component analysis [31] are still linear). Principal components (PCs) are extracted from the vectors in X and are the compact representation of the basis vectors while $K < p$ (this is also used for key wavelength identification in detecting ochratoxin A (OTA) contamination in wheat using near infrared (NIR) [32]).

This is not the first time that sparse computation is used in spectral analysis ([33, 34, 35]). However, previous research was related to unmixing and endmem-

ber analysis in hyperspectral remote sensing imagery, which differs from the perspectives of this paper. The regularization terms were imposed for mathematically solving sparse unmixing in three types of methods, namely, convex relaxation methods [33, 34], greedy algorithms [36] and sparse Bayesian methods [35], but we use it to extract spectral references through the first basis attained by Sparse-PCA calculation. The replacement of the non-smooth l_0 with l_1 or l_p norm imposes the well-defined optimization problems to a tractable solution [37] in the convex relaxation methods: e.g. the alternating direction method of multiplier method [38, 39]. The l_0 regularization problem in the greedy algorithm is solved by an iterative identification of potential endmembers from the spectral library until the advent of best reconstruction in the mixed pixel [37]. Sparse-PCA involves additional regularization parameters, which maximize the uncorrelated PC variance and convert PCA into nonlinear transformation [30, 40]. The Sparse-PCA elastic net has relaxation l_2 and l_1-penalty terms as follows:

$$\{\hat{\zeta}_k, \hat{\gamma}_k\} = argmin_{\zeta_k} \|X - X\gamma_k\zeta_k^T\|_F^2 + \delta\|\gamma_k\|_2^2 + \lambda\|\gamma_k\|_1,$$

$$\textbf{s. t.} \quad \mathrm{A}_k^T A_k = I. \quad (2)$$

where X_{ζ_k} is the response vector, $\hat{\gamma}_k = (X^T X + \delta I)^{-1} X^T X_{\zeta_k}$, and $\hat{\zeta}_k = argmin_{\zeta_k} \|X - X\gamma_k\zeta_k^T\|_F^2 \textbf{s.t.} \zeta_k^T\zeta_k = 1, \zeta_k^T A_{(k-1)} = 0$. In the case where the l_2 regularization parameter δ is changing, the second term of the equation above would be influenced (the γ_k approximation can be done by a soft-thresholding rule [30]). γ_k^1 represents sparse calculated eigenvector corresponds to the highest eigenvalue which designates higher dominating spectra in the sparse basis matrix. Sparse-PCA was employed to unmixed sampled spectra to extract spectral references. This experiment involved two types of grain samples: the group that did not exhibit any aggregation with other minerals (called 'pure samples') and other samples in which several grain types were mixed with other grains (e.g. quartz). By applying Sparse-PCA to the spectra of pure samples, we extracted the spectra for use as spectral reference (it can replace ASTER or USGS

spectral libraries) in the application of spectral comparison techniques (as the classification attributes). For example, in SAM, the spectral angle between the low rank Sparse-PCA spectra and every other pixel spectra in the image cube was calculated to provide the attributes that were used in the classification step [41].

2.2. Segmentation

Segmentation is essential to identify the minerals, and it can be performed by simple approaches such as spectral information segmentation and discrimination ratio (threshold) or applying sophisticated techniques such as ELM or K-means clustering. This section briefly reviews the methods employed for segmentation

Extreme Learning Machine (ELM)

Artificial neural networks can estimate difficult nonlinear mappings from the input sample. A single layer feed-forward network structural design called ELM was proposed by Huang et al. [42], which solves the initiation problem when using gradient descent. This technique reduces the computational complexity for training, enhances learning performance compared with conventional approaches and is capable of nonlinear kernel and activation functions [43].

Clustering

To cluster hyperspectral image cubes obtained from the experiments in an unsupervised way, huesaturationvalue (HSV)-based K-means clustering was used. This method categorizes false colors created to different groups, where these groups are labeled as different minerals using spectral comparison techniques. In general, false color composites are obtained by placing parts of wavelengths in different color groups (around the wavelengths of 1150 μm = red; 960 μm = green; 1060 μm = blue). However, in this study, we obtained them through spectral comparison techniques by applying different values of spectral comparison attributes into a specific color (for example SAM_{pyrope} = red, $SAM_{olivine}$ = green, and SAM_{quartz} = blue).

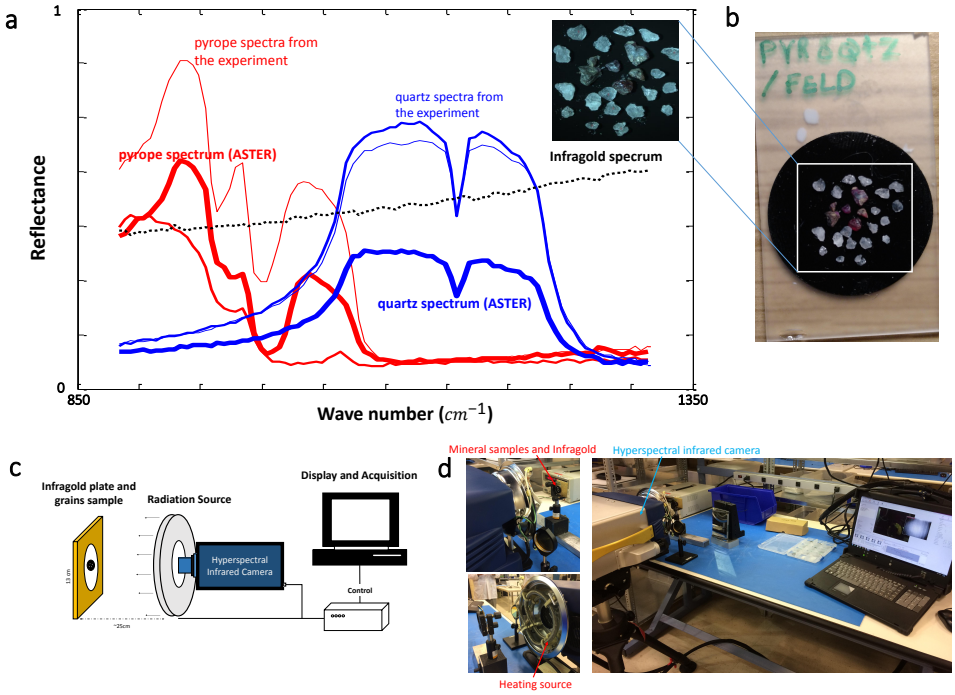

Figure 2: Experimental setup and spectra of minerals are shown in the figure. Upper image represents the spectra of the minerals used in the experiment (pyrope and quarts mixed sample) along with spectra from ASTER spectral library (**a,b**). Lower left hand-side image is the scheme of experimental setup (**c**) along with three pictures taken from the conducted experiment (**d**).

3. Experimental Results

The proposed approach is based on statistical analysis and computer simulations on hyperspectral data. The properties of the dataset, acquisition properties and experimental setup are described.

3.1. Mineral Grains and LWIR spectroscopy

Given that the field of view (FOV) of the sensor was small and the grains were between 0.6 and 2.0 mm, a special lens was used for higher spatial resolution (which is described in the subsequent section). The mineral samples

were divided into groups of mixed and pure samples, and three minerals presented distinguishable spectra in LWIR (i.e. Olivine $(Mg^{+2}, Fe^{+2})_2SiO_4$, Pyrope $Mg_3Al_2(SiO_4)_3$ and Quartz SiO_2 [44]). Figures 2a and 2b show the spectra of a mineral and one example of a mixed sample. Image acquisition in this paper was conducted while the heating source was turned on and off (for performing the continuum removal [45]). For both conditions, the spatial resolution was 200×256, and 87 spectral channels were recorded. The sensor used to make the measurements was a lightweight hyper-camera imaging spectroradiometer (HYPER-CAM LW) [46] operating in the LWIR band (from 7.7 to 11.8 μm). The LWIR PV-MCT focal plane array detector has a spatial resolution of 320×256 and spectral resolution up to $0.22\mu m$. The spectra were obtained using a Fouriertransform spectrometer, and the hyper-camera measured the complete spectrum for every pixel and had an instantaneous FOV of 0.35 mrad [46]. An LW macro lens provided a pixel footprint of 0.1 mm with working distance of 30 cm (Figure 2b). A heating source was located in front of the samples to provide active thermographical conditions in the experiment (Figure 2c). However, image acquisition was continued after turning off the heating source. The grains were attached to adhesive carbon-based tape during the experiment and then placed on an infra-gold plate. The hyperspectral images were obtained perpendicularly with the spectral resolution of 6 cm^{-1} ($\sim 0.0119\mu m$ at $7.7\mu m$ and $\sim 0.0465\mu m$ at 11.8 μm) in 87 spectral bands. Given that an infragold was placed in the background, its reflectance assisted in removing the continuum from the spectrum [45].

3.2. Results of proposed approach

The results of the proposed approach are presented in this section, and they are divided into two stages. Firstly, the results of the application of low rank Sparse-PCA from the pure samples versus ASTER spectral library as the reference spectra in spectral comparison techniques are demonstrated. Secondly, the results of using two different learning systems are analyzed.

3.3. ASTER spectral library and the result of Sparse-PCA as reference spectra

The ASTER imaging program at NASA [4] comprises compilations of spectral information from the Jet Propulsion Laboratory, Johns Hopkins University and the United States Geological Survey. The library contains the spectra of nearly 2000 types of soils, rocks, minerals, snow, water and artificial minerals. Several of these spectra cover the wavelengths measured in this study (0.4 14 μm). The spectral data for each mineral cover the visible, NIR, mid-IR and thermal IR wavelengths. To apply the spectral comparison techniques, the spectral reference has a key role in the calculations. In general, the ASTER spectral library is used as a reference spectrum for each mineral. Here, the possibility of using Sparse-PCA as spectral reference was analysed by generating the spectral references from pure mineral grains. PCA itself can provide a reasonable representation of the statistical information, but Sparse-PCA provides more robust data facing noise [36, 33, 34, 37, 38, 39, 30, 40]). The low rank Sparse-PCA spectra extracted from the basis matrix (sparse calculated eigenvector matrix) having the spectra of pure samples as their input and the abundance spectra of pure samples usually belong to one mineral. The extracted spectra (low rank Sparse-PCA spectra) also belong to the same mineral and used as reference spectra. The results are confirmed by comparing the ASTER spectra with the low rank Sparse-PCA spectra, which show identical similarity (Table 1) and using SAM and NCC [1]. To calculate the reference spectra using Sparse-PCA, a pixel spectra set of pure sample minerals was used as a training set with no overlap to the testing set (testing sets contained pyrope-quartz or olivine-quartz grain-mixed samples).

[1] This calculation is simply a score of difference, and it differs from using spectral comparison for generation classification attributes or false color images.

Table 1: Comparison among the low rank Sparse-PCA spectral references and ASTER mineral spectra using SAM and NCC (percentage of the similarity).

Spectral Comparison Technique	Quartz	Quartz Similarity (%)	Olivine	Olivine Similarity (%)	Pyrope	Pyrope Similarity (%)
SAM	0.4830	51.70	0.2698	73.02	0.2330	76.70
NCC	0.6055	60.55	0.9336	93.36	0.9520	95.20

3.4. Segmentation performance

3.4.1. Results of spectral comparison techniques

The performance of the spectral comparison techniques is presented in this section. SAM and NCC demonstrated higher performance than SID due to the direct calculation of the difference between the targeted and referenced spectra. These algorithms calculate the difference between the reference and targeted spectra, and this difference is given in the form of an error (in the case of SAM-lesser error shows better fitting), correlation similarity (in the case of NCC-higher score shows better fitting) and cross entropy (in the case of SID-higher entropy depicts better correlation). Topological similarities among the mineral's spectra create sufficient performance for SAM and NCC due to their dependency on the shape of the spectra as compared with SID, which estimates the difference entropy based on statistical information. Moreover, applying spectral comparison techniques showed good improvement in generating false colors, which led to better identification of the minerals using clustering (Figure 4). The main reason behind this improvement is elimination of unrelated parts of the spectrum, which decrease inconsistencies between the target and reference spectra. Each pixel spectrum was compared to provide the spectral difference for targeted pixel spectrum and continued by looping over all the spectral pixels in the hyperspectral cube. Consequently, spectral variation provides a map that represents the similarity of the spectra to the targeted spectra (i.e. a

Table 2: Accuracy of ELM for mineral identification.

Minerals		Spatial resolution of RoI	Accuracy of Classification (%)							
			ELM							
			Linear kernel		Polynomial kernel		RBF		Sigmoid	
			SAM	NCC	SAM	NCC	SAM	NCC	SAM	NCC
background	Pyrope	160*161	99.8	98.9	99.9	99.4	99.9	99.1	99.9	99.1
	Olivine	157*139	94.1	98.4	97.2	99.9	95.5	99.9	92.5	98.8
Non-background	Pyrope	160*161	97.7	10	99.1	43.35	98.95	10	98.95	10
	Olivine	157*139	94.8	87.95	97.7	99.55	96.3	99.05	93.55	93.65

Table 3: Computational load for ELM classification is shown.

Minerals	Spatial resolution of RoI	Spectral comparison techniques		Computational Cost (time in second)							
				ELM							
				Linear kernel		Polynomial kernel		RBF		Sigmoid	
				Training Time	Testing Time	Training Time	Testing Time	Training Time	Testing Time	Training Time	Testing Time
Pyrope	160*161	SAM	21.16	63.10	0.61	71.91	7.67	65.68	4.06	126.07	3.08
		NCC	27.74	59.83	0.68	73.68	7.67	64.95	4.15	119.55	3.02
Olivine	157*139	SAM	20.64	55.63	0.61	66.16	6.98	61.99	3.93	107.09	2.71
		NCC	26.89	54.61	0.64	64.18	7.07	57.65	3.76	110.41	3.02

false color map). These metrics are the input for the segmentation section in the approach and used as classification attributes or false color images to be grouped in different sets.

3.4.2. Results of ELM and clustering

The minerals were identified in different settings involving supervised/unsupervised approaches. For the supervised approach, a training set was randomly selected from pixels of mineral grains. By contrast, the unsupervised approach did not require a training stage, but the selection of the clusters needed interference of training information (labeled data). Before explaining the performance of segmentation, we analyzed the performance of spectral comparison techniques. Spectral comparison techniques provided the classification attributes and false color images, which facilitated the classification and clustering segmentation

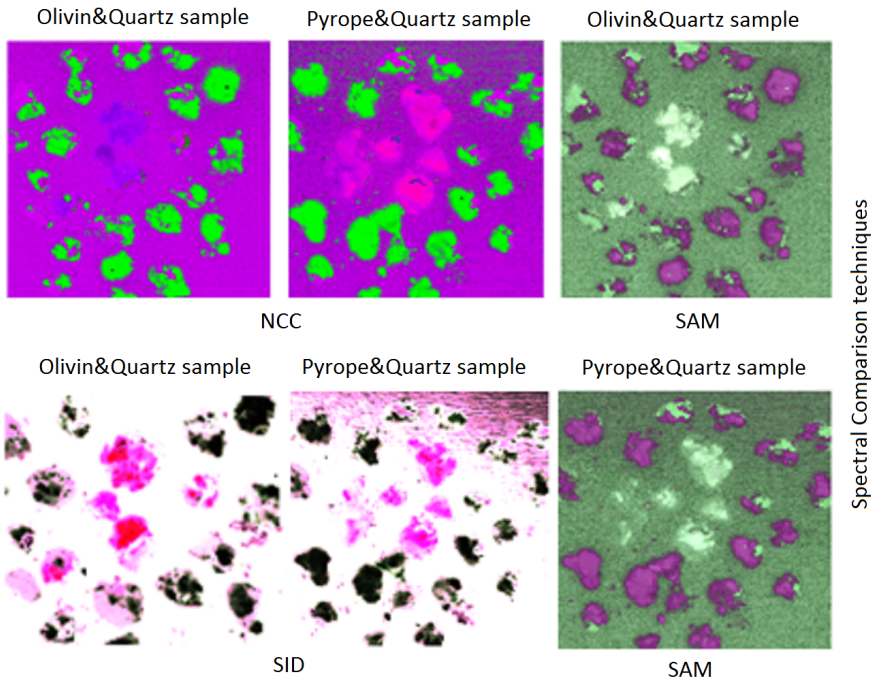

Figure 3: The results of spectral comparison analysis (SAM, SID, and NCC) are revealed by false colors in the figure.

of mineral grains in the hyperspectral images, respectively. The results of different segmentation methods to identify minerals are shown. Two techniques, namely, ELM and K-means clustering, were tested. Three different minerals displayed varying signatures in the LWIR band and spectra corresponding to the sample's background. Consequently, four different classes, including the background, were explored in the hyperspectral images for the presence of alternative classification/clustering methods.

Automated mineral identification using ELM classification followed the training and testing scenario. Classification with ELM [with linear, polynomial, radial-based function and Sigmoid kernels][42, 43, 47, 48] was directly related to the training stage. Training and testing were conducted based on the feature values

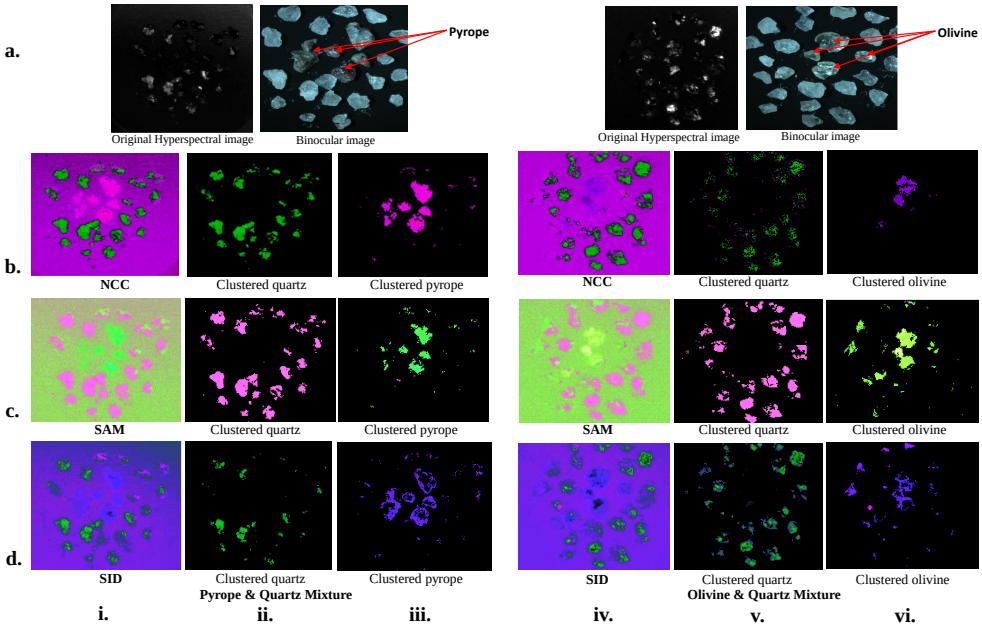

Figure 4: The results of the clustering by SAM (**a.**), NCC (**b.**), and SID (**c.**). The mineral grains have been automatically detected through their false colors. **a.** and **b.** show the hyperspectral and binocular images from olivine and pyrope, respectively. Columns **i.** and **iv.** show the false colors results using the spectral comparison techniques. Columns **ii.**, **iii.**, **v.**, and **vi.** depict the clustering results for each minerals and every spectral methods.

of NCC and SAM as the attributes were separately calculated for each mineral. The number of observations for every spectral analysis and mineral differed due to extra enhancing filtering, which was performed to eliminate inconsistency in the training and testing data (between 1000-3000 and 800 non-overlapping samples for training and testing, respectively) [49]. Tables 2 and 3 show the accuracy and computational load for ELM classification.

The unsupervised segmentation of minerals was performed by HSV color-based K-means clustering. The entire processes of clustering were executed knowing the number of interested clusters and the relevant data to select a particular cluster. The results of HSV-based K-mean clustering are shown in Figure 4. Given that the accuracy of the clustering techniques in Table 4 is directly re-

Table 4: Accuracy of the HSV based clustering for three different samples.

MAM	HSV-based clustering	Quartz (%)	Pyrope (%)	Olivine (%)	Total accuracy (%)
NCC	Accuracy of mineral detection	77.95	94.59	85.39	85.98
	Misclassification	22.06	5.41	14.61	14.02
	Total accuracy	55.89	89.19	70.78	71.95
SAM	Accuracy of mineral detection	75.82	91.40	99.75	88.99
	Misclassification	29.56	29.34	4.03	20.98
	Total accuracy	46.25	62.06	95.72	68.01
SID	Accuracy of mineral detection	68.52	72.01	92.19	77.57
	Misclassification	31.48	27.99	7.81	22.43
	Total accuracy	37.04	44.01	84.38	55.14

lated to the accuracy of segmentation using clustering, global accuracy of the approaches was calculated by multiplying the accuracy of each step by the segmentation results. Table 5 shows the computational complexity of false color generation and applying clustering for mixed sample sets. The entire computational process was performed with a PC (Intel Core 2Quad CPU, Q6600, 2.40 GHz, RAM 8.00 GB, 64 bit Operating System), and data analysis was conducted using MATLAB programming language. To apply these techniques, a MATLAB hyperspectral image index analysis toolbox [50] was used. Figure 4 depicts the segmentation results through clustering. Given the similarity between low rank Sparse-PCA and ASTER (Table 1), either the low rank Sparse-PCA spectra or the ASTER library data could be used as the reference spectrum. Table 1 represents an estimation of the spectral similarity among the spectra in percentage. It indicates the sensitivity of the spectral comparison methods used for spectral comparison calculation.

Table 5: Computational complexity of the false color generation and clustering approach.

Computational Cost (time in second)				
Minerals	**Spatial Resolution**	**NCC**	**SAM**	**SID**
Mixture of Pyrope & Quartz	144*152	362.3	325.4	354.2
Mixture of Olivine & Quartz	157*139	497.7	331.3	368.6

3.4.3. Accuracy of the classification

The proposed approach provided accuracy by counting the correct detected pixels of hyperspectral images. Ground truth was required to compare the results of systems for quantitative assessment. Ground truth was made by manually labeling the images for different types of minerals. The labeled images were verified using micro X-ray fluorescence (μXRF) images from the samples and ArcGIS to map them with the labeled images or with results of automatic detection (Figures 5 and 6). The ground truth was prepared using the information of mineral aggregate obtained by μXRF test. Since the aggregation information depends on mineral content in every sample, the labeling process is facilitated considering the results of μXRF for particular element(s) in each grain. Figure 6 depicts the process of creating ground truth image for biotite sample. Since biotite contains several distinctive elements such as Mg, Ti, Fe, Al, etc and their maps guide the biotite labeling in the reference image. Similarly for quartz, that the aggregate of Si guides the quartz ground truth to be labeled. Local accuracy (ACC) is calculated by:

$$ACC(\%) = \frac{Correct\ detected\ pixels}{Total\ pixels\ of\ mineral} * 100 \tag{3}$$

Notably, the location of the detected pixels is vital to identify the mineral grains. The total accuracy of both methods was calculated. The total accuracy of each method was multiplied by the sensitivity percentage of spectral comparison techniques (Table 1), which might decrease the current accuracy. However, the accuracy did not indicate the reliability of the system because the main objective was to identify the grains. Pixel calculation was performed as a

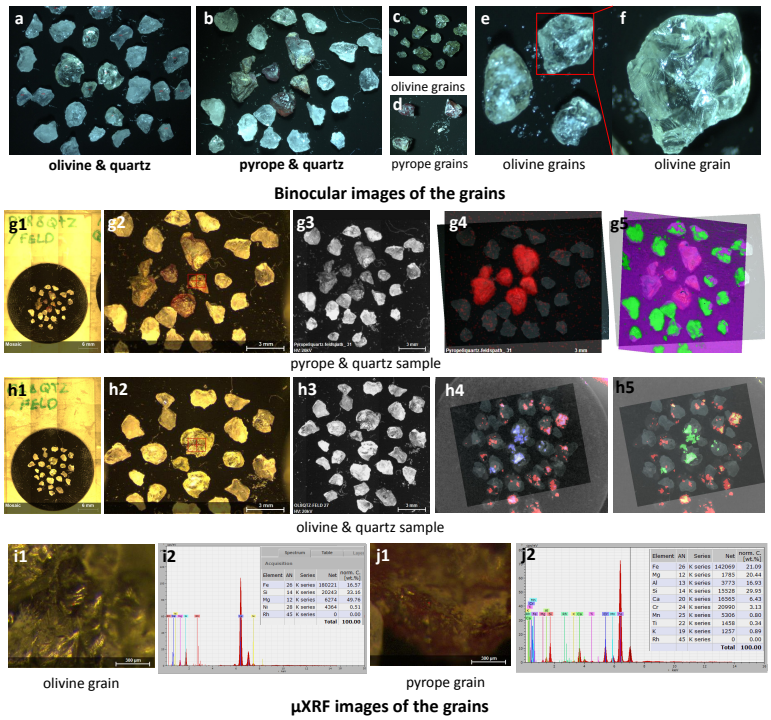

Figure 5: The binocular images from the grains of pyrope, olivine, and mixed with quartz grains are shown. Also the /muXRF image of the samples are also shown in the image to verify the ground truth images and labeling. (**g1-g3** and **h1-h3** depict the images of pyrope-quartz and olivine-quartz samples using Micro X-ray fluorescence (μXRF), respectively. **i1,i2,j1,j2** show a point in the grains of olivine and pyrope, respectively.

comparison criterion, and two or three pixels in the grains provided satisfactory outcomes for the system (as these pixels represent the grain's content).

4. Discussion

The main objective of this research was to compare two automatic methods for mineral identification. For this purpose, we used statistical and spectral information for hyperspectral comparison analysis. Segmentation and mineral identification in the hyperspectral images underlined a set of feature combinations using such information. This study has shown the application of hy-

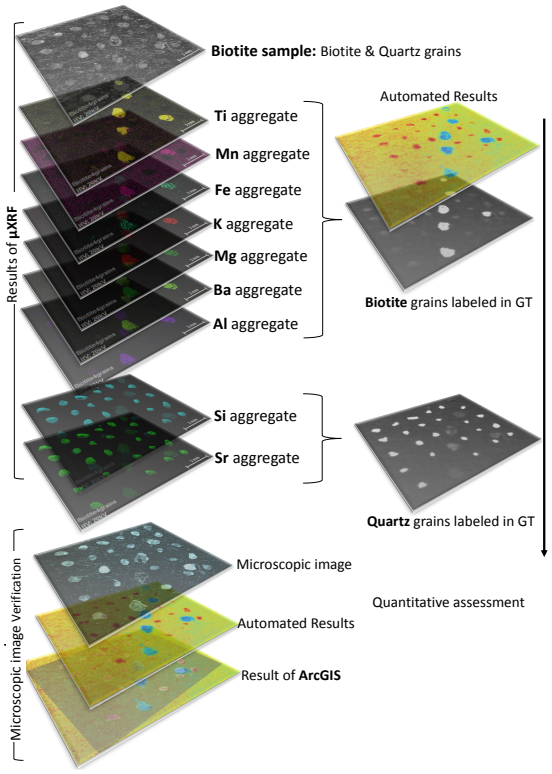

Figure 6: The image presents the procedure of creating the ground truth images as the reference for our computational and quantitative analysis. μXRF shows the mineral aggregate for the grains in the sample which led to creating the labeled reference images for biotite and quartz (upper part of the figure). In addition, ArcGIS fitted the microscopic image of the samples with the results of automated identification (lower part of the figure).

perspectral infrared imagery in the 7.711.8 μm wavelength range for mineral identification through supervised/unsupervised categorization techniques. The presented approach challenged two different types of segmentation involving classification (using SAM and NCC) and clustering (using SAM, SID and NCC). As the classification is a supervised approach, it suffers from dependency on the number of training samples in the training stage. Misclassifications are ultimately inevitable because of the small size of grains and lack of proper training in the system. Moreover, the nature of the classification approach unequivocally

creates two stages of data processing, which is considered an inauspicious shortcoming that debilitates supervised system versus unsupervised system (particularly for this application). In addition, application of the supervised procedure (e.g. ELM) might create too much sensitivity against acquisition's parameters, such as experimental setup, background or special temperature of heating source. This disadvantage might be attributed by specific values of weights in the training matrix (in the case of using ELM or any other neural networks). On the contrary, clustering leads a direct grouping of spectral data and is simple and propitious to be used for such applications. It does not involve a training stage, which considerably decreases pre-processing analysis and labeling costs, but it is also highly robust against acquisition parameters. This work considered limited mixed samples (quartz, pyrope, and olivine) to focus more on the comparison analysis of supervised and unsupervised machine learning approaches and avoid obfuscating the discrimination problem. However, each of these approaches can be modified and challenged by more complicated scenarios to verify their strength and shortfalls.

The contributions of the proposed approach can be examined through two major points of view: geological and spectral analysis. In geology, the presented method increased the perspective of mineral identification from remote sensing, airborne imagery and core logging to the small mineral grains, which includes the analysis for estimation of spectral radiation (continuum removal) and identification computations. Some related works include hyperspectral mineral identification in core logging (i.e. [12, 13, 14]), which was highly similar to the method in this research in terms of close range (distance between target and hyperspectral camera) and experimental conditions. However, their complex mineral aggregate and shape of mineral targets were comparatively different. The second point of the contribution is related to a major comparison between the two methods for automation of mineral identification and spectral analysis. ELM and clustering approaches were compared for the same sample sets.

5. Conclusions

The presented approach involved an experiment in the hyperspectral imagery in the 7.7μm to 11.8μm LWIR wavelength range conducted using a FTIR hyperspectral camera. The objective was automatic identification of certain minerals (pyrope, olivine and quartz). Spectral comparison methods such as SAM, SID and NCC have been used to extract features in the form of false colors. Spectral references provided by statistical information using Sparse-PCA to extract the low rank Sparse-PCA from pure sample grains. These spectral references have shown identical similarity compared with ASTER (JPL/NASA) spectral library. For final decision making, two approaches were investigated (i.e. ELM and HSV-based K-means clustering) to identify the mineral grains in a supervised/unsupervised manner, and the results indicated promising accuracy. Comparisons could be made by keeping the study limitations in mind, such as the non-homogeneous surface of mineral grains that creates the radiometric variation as changing parameters within the test. The supervised classification accuracy reached 76.69% using SAM-based polynomial kernel ELM for pyrope mixture and 70.95% using SAM-based sigmoid kernel ELM for olivine mixture as overall hyperspectral image classification accuracy. The classification accuracy was slightly lower than that of clustering, which exhibited an accuracy of 84.91% (NCC) for pyrope and 69.9% (SAM) for olivine identification by adding the sensitivity percentage into the accuracy calculations. The supervised classification showed significant dependency on the number of training samples and was considerably more difficult than clustering. The results of SID showed lower efficiency than those of SAM and NCC. Future work requires further analysis to increase the performance of automatic identification of mineral grains.

Acknowledgment

The authors would thank anonymous reviewers and editor of Infrared Physics & Technology journal for their constructive comments. Also we would like to ac-

knowledge and thank Annette Schwerdtfeger from the Department of Electrical and Computer Engineering at Laval University for her constructive comments and help. This research was supported by FRQ-NT (Fonds de Recherche du Québec - Nature et Technologies) grant number: 2014-MI-182452 and conducted under the Canadian tier 1 research chair in Multipolar Infrared Vision (MIVIM) and the Chaire de recherche industrielle CRSNG- Agnico-Eagle en exploration minérale.

Conflicts of Interest: The authors declare no conflict of interest.

References

[1] B. Yousefi, S. Sojasi, C. I. Castanedo, X. P. Maldague, G. Beaudoin, M. Chamberland, Comparison assessment of low rank sparse-pca based-clustering/classification for automatic mineral identification in long wave infrared hyperspectral imagery, Infrared Physics & Technology`doi:10.1016/j.infrared.2018.06.026`.

[2] A. F. Goetz, Three decades of hyperspectral remote sensing of the earth: A personal view, Remote Sensing of Environment 113 (2009) S5–S16.

[3] F. D. Van der Meer, H. M. Van der Werff, F. J. van Ruitenbeek, C. A. Hecker, W. H. Bakker, M. F. Noomen, M. van der Meijde, E. J. M. Carranza, J. B. de Smeth, T. Woldai, Multi-and hyperspectral geologic remote sensing: A review, International Journal of Applied Earth Observation and Geoinformation 14 (1) (2012) 112–128.

[4] A. Baldridge, S. Hook, C. Grove, G. Rivera, The aster spectral library version 2.0, Remote Sensing of Environment 113 (4) (2009) 711–715.

[5] I. Entezari, B. Rivard, M. Geramian, M. G. Lipsett, Predicting the abundance of clays and quartz in oil sands using hyperspectral measurements, International Journal of Applied Earth Observation and Geoinformation 59 (2017) 1–8.

[6] J. Feng, B. Rivard, D. Rogge, A. Sanchez-Azofeifa, The longwave infrared (3–14μm) spectral properties of rock encrusting lichens based on laboratory spectra and airborne sebass imagery, Remote Sensing of Environment 131 (2013) 173–181.

[7] E. Cloutis, Review article hyperspectral geological remote sensing: evaluation of analytical techniques, International Journal of Remote Sensing 17 (12) (1996) 2215–2242.

[8] A. Plaza, J. A. Benediktsson, J. W. Boardman, J. Brazile, L. Bruzzone, G. Camps-Valls, J. Chanussot, M. Fauvel, P. Gamba, A. Gualtieri, et al., Recent advances in techniques for hyperspectral image processing, Remote sensing of environment 113 (2009) S110–S122.

[9] R. J. Murphy, S. Schneider, S. T. Monteiro, Consistency of measurements of wavelength position from hyperspectral imagery: Use of the ferric iron crystal field absorption at 900 nm as an indicator of mineralogy, IEEE Transactions on Geoscience and Remote Sensing 52 (5) (2014) 2843–2857.

[10] C. Deng, S. Zhang, S. Wang, W. Tian, Z. Wu, Sparse hyperspectral unmixing based on smoothed 0 regularization, Infrared Physics & Technology 67 (2014) 306–314.

[11] X. Wan, C. Zhao, Y. Wang, W. Liu, Stacked sparse autoencoder in hyperspectral data classification using spectral-spatial, higher order statistics and multifractal spectrum features, Infrared Physics & Technology 86 (2017) 77–89.

[12] F. Kruse, Identification and mapping of minerals in drill core using hyperspectral image analysis of infrared reflectance spectra, International journal of remote sensing 17 (9) (1996) 1623–1632.

[13] W. M. Calvin, E. L. Pace, Mapping alteration in geothermal drill core using a field portable spectroradiometer, Geothermics 61 (2016) 12–23.

[14] M. Tappert, B. Rivard, D. Giles, R. Tappert, A. Mauger, Automated drill core logging using visible and near-infrared reflectance spectroscopy: a case study from the olympic dam iocg deposit, south australia, Economic Geology 106 (2) (2011) 289–296.

[15] J. Crowley, D. Williams, J. Hammarstrom, N. Piatak, I.-M. Chou, J. Mars, Spectral reflectance properties (0.4–2.5 μm) of secondary fe-oxide, fe-hydroxide, and fe-sulphate-hydrate minerals associated with sulphide-bearing mine wastes, Geochemistry: Exploration, Environment, Analysis 3 (3) (2003) 219–228.

[16] R. V. Morris, H. V. Lauer, C. A. Lawson, E. K. Gibson, G. A. Nace, C. Stewart, Spectral and other physicochemical properties of submicron powders of hematite (α-fe2o3), maghemite (γ-fe2o3), magnetite (fe3o4), goethite (α-feooh), and lepidocrocite (γ-feooh), Journal of Geophysical Research: Solid Earth 90 (B4) (1985) 3126–3144.

[17] A. C. Scheinost, D. G. Schulze, U. Schwertmann, Diffuse reflectance spectra of a1 substituted goethite: A ligand field approach, Clays and Clay Minerals 47 (2) (1999) 156–164.

[18] J. Feng, D. Rogge, B. Rivard, Comparison of lithological mapping results from airborne hyperspectral vnir-swir, lwir and combined data, International Journal of Applied Earth Observation and Geoinformation.

[19] R. N. Clark, T. V. King, M. Klejwa, G. A. Swayze, N. Vergo, High spectral resolution reflectance spectroscopy of minerals, Journal of Geophysical Research: Solid Earth 95 (B8) (1990) 12653–12680.

[20] R. Murphy, The effects of surficial vegetation cover on mineral absorption feature parameters, International Journal of Remote Sensing 16 (12) (1995) 2153–2164.

[21] R. Clarke, Chapter 1: Spectroscopy of rocks and minerals, and principles

of spectroscopy, manual of remote sensing, remote sensing for the earth sciences (pp. 3–58) (1999).

[22] R. N. Clark, T. L. Roush, Reflectance spectroscopy: Quantitative analysis techniques for remote sensing applications, Journal of Geophysical Research: Solid Earth 89 (B7) (1984) 6329–6340.

[23] B. Yousefi, S. Sojasi, C. I. Castanedo, X. P. Maldague, G. Beaudoin, M. Chamberland, Continuum removal for ground based lwir hyperspectral infrared imagery applying non-negative matrix factorization.

[24] R. N. Clark, G. A. Swayze, K. E. Livo, R. F. Kokaly, S. J. Sutley, J. B. Dalton, R. R. McDougal, C. A. Gent, Imaging spectroscopy: Earth and planetary remote sensing with the usgs tetracorder and expert systems, Journal of Geophysical Research: Planets 108 (E12).

[25] J. M. Sunshine, C. M. Pieters, Estimating modal abundances from the spectra of natural and laboratory pyroxene mixtures using the modified gaussian model, Journal of Geophysical Research: Planets 98 (E5) (1993) 9075–9087.

[26] R. N. Clark, G. A. Swayze, Mapping minerals, amorphous materials, environmental materials, vegetation, water, ice and snow, and other materials: the usgs tricorder algorithm.

[27] F. Kruse, A. Lefkoff, J. Boardman, K. Heidebrecht, A. Shapiro, P. Barloon, A. Goetz, The spectral image processing system (sips)interactive visualization and analysis of imaging spectrometer data, Remote sensing of environment 44 (2) (1993) 145–163.

[28] Center for the study of earth from space (cses), SIPS User's Guide, The Spectral Image Processing System 1.1 (1992) 74p.

[29] C.-I. Chang, Spectral information divergence for hyperspectral image analysis, in: Geoscience and Remote Sensing Symposium, 1999. IGARSS'99 Proceedings. IEEE 1999 International, Vol. 1, IEEE, 1999, pp. 509–511.

[30] H. Zou, T. Hastie, R. Tibshirani, Sparse principal component analysis, Journal of computational and graphical statistics 15 (2) (2006) 265–286.

[31] J. Huang, Y. Ma, X. Mei, F. Fan, A hybrid spatial-spectral denoising method for infrared hyperspectral images using 2dpca, Infrared Physics & Technology 79 (2016) 68–73.

[32] T. Senthilkumar, D. Jayas, N. White, P. Fields, T. Gräfenhan, Detection of ochratoxin a contamination in stored wheat using near-infrared hyperspectral imaging, Infrared Physics & Technology 81 (2017) 228–235.

[33] M.-D. Iordache, J. M. Bioucas-Dias, A. Plaza, Total variation spatial regularization for sparse hyperspectral unmixing, Geoscience and Remote Sensing, IEEE Transactions on 50 (11) (2012) 4484–4502.

[34] M.-D. Iordache, J. M. Bioucas-Dias, A. Plaza, Collaborative sparse regression for hyperspectral unmixing, Geoscience and Remote Sensing, IEEE Transactions on 52 (1) (2014) 341–354.

[35] K. E. Themelis, A. A. Rontogiannis, K. D. Koutroumbas, A novel hierarchical bayesian approach for sparse semisupervised hyperspectral unmixing, Signal Processing, IEEE Transactions on 60 (2) (2012) 585–599.

[36] M.-D. Iordache, J. M. Bioucas-Dias, A. Plaza, Sparse unmixing of hyperspectral data, Geoscience and Remote Sensing, IEEE Transactions on 49 (6) (2011) 2014–2039.

[37] J. A. Tropp, S. J. Wright, Computational methods for sparse solution of linear inverse problems, Proceedings of the IEEE 98 (6) (2010) 948–958.

[38] M. V. Afonso, J. M. Bioucas-Dias, M. A. Figueiredo, An augmented lagrangian approach to the constrained optimization formulation of imaging inverse problems, Image Processing, IEEE Transactions on 20 (3) (2011) 681–695.

[39] S. Mei, Q. Du, M. He, Equivalent-sparse unmixing through spatial and spectral constrained endmember selection from an image-derived spectral library, Selected Topics in Applied Earth Observations and Remote Sensing, IEEE Journal of 8 (6) (2015) 2665–2675.

[40] K. Sjöstrand, L. H. Clemmensen, R. Larsen, B. Ersbøll, Spasm: A matlab toolbox for sparse statistical modeling, Journal of Statistical Software.

[41] B. Yousefi, S. Sojasi, C. I. Castanedo, G. Beaudoin, F. Huot, X. P. Maldague, M. Chamberland, E. Lalonde, Mineral identification in hyperspectral imaging using sparse-pca, in: Thermosense: Thermal Infrared Applications XXXVIII, Vol. 9861, International Society for Optics and Photonics, 2016, p. 986118.

[42] G.-B. Huang, Q.-Y. Zhu, C.-K. Siew, Extreme learning machine: a new learning scheme of feedforward neural networks, in: Neural Networks, 2004. Proceedings. 2004 IEEE International Joint Conference on, Vol. 2, IEEE, 2004, pp. 985–990.

[43] R. Rajesh, J. S. Prakash, Extreme learning machinesa review and state-of-the-art, International journal of wisdom based computing 1 (1) (2011) 35–49.

[44] http://mindat.org (2012).

[45] B. Yousefi, S. Sojasi, C. I. Castanedo, G. Beaudoin, F. Huot, X. P. Maldague, M. Chamberland, E. Lalonde, Emissivity retrieval from indoor hyperspectral imaging of mineral grains, in: Thermosense: Thermal Infrared Applications XXXVIII, Vol. 9861, International Society for Optics and Photonics, 2016, p. 98611C.

[46] Telops, http://telops.com/products/hyperspectral-cameras/item/ (2016).

[47] G.-B. Huang, L. Chen, C.-K. Siew, Universal approximation using incremental constructive feedforward networks with random hidden nodes, Neural Networks, IEEE Transactions on 17 (4) (2006) 879–892.

[48] B. Yousefi, C. K. Loo, Slow feature action prototypes effect assessment in mechanism for recognition of biological movement ventral stream, International Journal of Bio-Inspired Computation 8 (6) (2016) 410–424.

[49] B. Yousefi, `http://vision.gel.ulaval.ca/~bardia/PublicCodes/WebJ1-19May2017.zip` (2016).

[50] Isaac, https://github.com/isaacgerg/matlabhyperspectraltoolbox (2015).